CORA Cork Open Research Archive
Cartlann Taighde Oscailte Chorcaí

Title	Alkaline earth metal oxide nanocluster modification of rutile TiO2 (110) promotes water activation and CO2 chemisorption
Authors	Nolan, Michael
Publication date	2018-05-01
Original Citation	Nolan, M. (2018) 'Alkaline earth metal oxide nanocluster modification of rutile TiO2 (110) promotes water activation and CO2 chemisorption', Journal of Materials Chemistry A, 6(20), pp.9451-9466. https://doi.org/10.1039/C8TA01789A
Type of publication	Article (peer-reviewed)
Link to publisher's version	http://dx.doi.org/10.1039/C8TA01789A - 10.1039/C8TA01789A
Rights	© The Royal Society of Chemistry 2018
Download date	2026-11-15 14:29:10
Item downloaded from	https://hdl.handle.net/10468/6043

UCC
University College Cork, Ireland
Coláiste na hOllscoile Corcaigh

Alkaline Earth Metal Oxide Nanocluster Modification of Rutile TiO_2 (110) promotes Water Activation and CO_2 Chemisorption

Michael Nolan[1]

Abstract

Metal oxide photocatalysts are widely studied for applications in solar driven environmental remediation, antimicrobial activity, hydrogen production and CO_2 reduction to fuels. Common requirements for each technology include absorption of visible light, reduced charge carrier recombination and the ability to activate the initial molecule be it a pollutant, water or CO_2. The leading photocatalyst is some form of TiO_2. A significant amount of work has been undertaken to modifying TiO_2 to induce visible light absorption. The structure and composition of the catalyst should facilitate separation of electrons and holes and having active sites on the catalyst is important to promote the initial adsorption and activation of molecules of interest. In this paper we present a first principles density functional theory (DFT) study of the modification of rutile TiO_2 (110) with nanoclusters of the alkaline earth metal oxides (MgO, Ca, BaO) and we focus on the effect of surface modification on the key catalyst properties. The modification of rutile TiO_2 with CaO and BaO induces a predicted red shift in light absorption. In all cases, photoexcited electrons and holes localise on oxygen in the nanocluster and surface Ti sites, thus enhancing charge separation. The presence of these non-bulk alkaline earth oxide nanoclusters provides highly active sites for water and CO_2 adsorption. On MgO-rutile, water adsorbs molecularly and overcomes a barrier of only 0.36 eV for dissociation whereby hydroxyls are stabilised. On CaO- and BaO-modified rutile water adsorbs dissociatively. We attribute this to the high lying O 2p states in the alkaline earth oxide modifiers which are available to interact with water, as well as the non-bulk like geometry around the active site. Upon adsorption of CO_2 the preferred binding mode is as a tridentate carbonate-like species, as characterised by geometry and vibrational modes. The carbonate is bound by up to 4 eV.

[1]*Tyndall National Institute, University College Cork, Lee Maltings Complex, Dyke Parade, Cork, Ireland, T12 R5CP*
michael.nolan@tyndall.ie
Electronic Supplementary Information (ESI) available: This includes transition state for water dissociation on $(MgO)_4$-rutile, the triplet electronic state for adsorbed CO_2 and a comparison of results with different place wave cut off energies See DOI: 10.1039/x0xx00000x

Thus these heterostructures can be interesting for CO_2 capture, helping alleviate the problem of CO_2 emissions.

Introduction

Metal oxide photocatalysts are of wide interest as low cost, environmentally friendly, earth abundant materials that can enable solutions for a number of technological and societal challenges. These include solar hydrogen production from water splitting[1-4], CO_2 reduction to hydrocarbons[5-21], and environmental remediation by the destruction of organic pollutants.[1, 22] Common to each technology are the requirements for the catalyst to be photoactive (ideally in the visible region), have reduced charge recombination and the ability to activate a feedstock molecule, such as water or CO_2. Engineering active sites on the photocatalyst is an interesting approach to enhance the adsorption and activation of molecules. This can be achieved by preparing well controlled nanoshapes of the oxides or by supporting nanoclusters on well-defined supports.

The most studied photocatalyst is titanium dioxide, TiO_2, which has many attractive properties including cost, non-toxicity and availability[1, 4, 7, 13, 22-24]. However, a major issue impeding the widespread use of TiO_2 in photocatalytic technologies is that the band gap of the common anatase and rutile polymorphs of TiO_2 lies in the UV region (E_g *ca.* 3.2 eV, depending on the crystal form). A significant amount of work has been published attempting to engineer the light absorption properties of TiO_2, primarily through substitutional cation or anion doping, so that the band gap lies in the visible region of the solar spectrum. This is supposed to enable the use of a larger fraction of the available solar energy than available in the UV [23, 25-53].

In these efforts, first principles density functional theory (DFT) simulations are extensively used in conjunction with experiment. This red shift generally arises from the introduction of new states in the original TiO_2 valence-conduction-band energy gap which then facilitates transitions between, e.g. dopant derived electronic states and empty TiO_2 states. Some experimental results on, e.g. N-doped TiO_2, indicate visible light absorption[31]. DFT simulations, have focused almost exclusively on band gap reduction due to doping[26, 29, 32, 33, 40, 41, 43, 44, 47, 48, 50-54], and neglect any detailed study of charge localisation and reactivity.

An alternative approach, which should be more robust than substitutional doping, is to exploit structural engineering of TiO_2, its composites and interfaces. A good example of a composite material is P25 which is used as the benchmark photocatalyst in many studies and is composed of a mix of rutile and anatase TiO_2 that are chemically interfaced, rather than being physically mixed. In terms of structure engineering, there has been great interest in synthesizing anatase TiO_2 structures with the (001) surface exposed, rather than the more stable (101) surface[55-60]. The motivation for this work is that the (001) anatase surface is more photocatalytically active than the (101) surface[55-60]. Wallace and McKenna[61] showed that different rutile facets display different charge trapping characteristics so that preparation of structures that expose particular rutile facets is an approach to tune charge localisation. Nanostructuring is another route to band gap and charge transport engineering, with nanostructures showing structure-dependent band gaps and providing short charge diffusion pathways that reduce recombination[62-64]. In addition, low coordinated metal and oxygen sites can be available for molecular adsorption.

Another approach is to fabricate heterostructures, which are composed of two different metal oxides or two different structures interfaced together, with the interface playing a key role. Recent results indicate that this heterostructuring approach is a successful and versatile approach to tune the structure to give visible light absorption and improved photocatalytic activity. Oxide-oxide structures such as $BiVO_4$-WO_3[65], TiO_2-WO_3[66], SnO_x-ZnGa2O4[67], SnO-TiO_2[68] and SnO-Zn_2SnO_4[69] and their interfaces display a band gap reduction, shifting the photoactivity into the visible region. These structures also promote electron/hole separation, to reduce charge recombination, giving improved photocatalytic activity over the pure oxides.

Combining the ideas of heterostructure formation and nanostructuring, Libera et al[70] and Tada et al.[24, 71, 72] showed that TiO_2 can be modified with sub-nm iron oxide nanoclusters. Both groups found greatly improved visible light activity and no impact on UV-light activity, which was postulated to arise from band gap narrowing due to the presence of the FeOx clusters shifting the top of the TiO_2 valence band[24, 70-72]. Photoluminescence spectroscopy showed a decrease in electron-hole recombination[72], characterised by a suppression in the PL peak of TiO_2 at 540nm after FeOx-modification.

Subsequent work has shown that a multitude of metal oxide nanocluster modifiers can be employed, including SnO_2, NiO[24, 73-75], SnO[68], and PbO[76] as further examples of

surface modified TiO_2 photocatalysts, with improved photoactivity and reduced charge recombination. Lobo and co-workers have also studied the modification of $ZnGa_2O_4$ with SnO/SnO_2[67].

While these structures show extremely good promise as novel photocatalysts, further work is needed to understand their fundamental properties and allow the development of surface modified TiO_2 catalysts. To illuminate the experimental studies and predict useful composite systems based on surface modification of TiO_2 with metal oxide nanoclusters, we have presented an extensive series of density functional theory (DFT) simulations of TiO_2 modified with a range of metal oxide nanoclusters; see refs. [24, 71, 77, 78]. These have not only confirmed the origin of band gap reduction in FeO_x modified rutile TiO_2[43], the origin of enhanced UV or visible light activity of SnO_2-modified anatase[41,42] or rutile[44] TiO_2 and the effect of NiO[75] or CuO[79] modification of rutile and anatase, but have also predicted composite systems with SnO[80] and PbO[81] nanocluster modification, both of which have been experimentally confirmed[68, 76]. We have further shown that the series ZnO, ZnS and ZnSe can be used to modify rutile TiO_2 to induce a band gap reduction[82] so that metal chalcogenides can be used to modify the light absorption properties of TiO_2.

In addition to the above analysis we have also studied a model of the photoexcited state, as first discussed by Di Valentin and Selloni[83], which allows us to predict the localisation of photoexcited electrons and hole. In the majority of metal oxide nanocluster modified TiO_2 systems the hole localises on low coordinated oxygen species in the nanocluster modifier and the electron on a single Ti site in the TiO_2 surface. The metal oxide nanoclusters present low coordinated oxygen and metal sites and it is the former that holes preferentially localize on. The model predicts red shift in light absorption and improved charge separation.

In further developing and understanding surface modified TiO_2, photocatalysts, it is necessary to examine the fundamental interactions of molecules at these heterostructured catalysts. Our choice of molecules is driven by potential applications of these catalysts; the molecules of interest are water and carbon dioxide which can be split into oxygen and hydrogen or activated and hydrogenated. If any of these molecules do not interact with the catalysts then no reaction takes place, and it does not matter what the properties of the potential photocatalyst are.

This paper presents a first principles DFT investigation of the interaction of water, CO_2 and H_2 at alkaline earth metal oxide nanocluster (MgO, CaO, BaO) modified rutile TiO_2

(110). In an earlier work we showed that MgO-modified rutile (110), has potentially useful photocatalyst properties[84]. The presence of a supported metal oxide nanocluster on the rutile (110) surface presents potentially active sites for molecular adsorption that are not available on the corresponding surfaces of the alkaline earth oxides or on rutile (110).

There has been a high level of interest in studying the interaction of water and CO_2 on alkaline earth metal oxide surfaces[85-101]. The interaction of water at oxide surfaces is always of interest due to the presence of atmospheric water under many conditions and the possibility of surface hydroxylation. In addition, water oxidation is a key and difficult step in the production of hydrogen from water on metal oxides. Alkaline earth oxides are basic and can adsorb CO_2 and are of interest in materials for CO_2 capture technologies where, for example, a strong oxide-CO_2 interaction facilitates the capture and storage of CO_2 emitted from an industrial process.

Water adsorption tends to be weak at the extended MgO (001) surface and dissociation is not particularly favourable, with a barrier of 1.09 eV[102]. On CaO and BaO (100) surfaces, water adsorption and dissociation are more favourable. In a series of papers Kawai et al.[90, 91, 102] investigated the interaction of water at ultrathin metal-supported MgO films and were able to explore differences between bulk-like and ultra-thin MgO. On MgO-Ag (100) the authors examined the role of interface defects[102] in promoting the initial adsorption of water, lowering the activation barrier and enhancing the stability of dissociated water. Interface O vacancies promoted water dissociation. In ref[90] a combined experimental and DFT modelling study of MgO-Ag(100) used STM to examine the spontaneous dissociation of water on the ultra-thin supported MgO. Here the ultra-thin MgO film does not notably change the initial water adsorption (energy gain of -0.46 eV on MgO (100) and -0.48 eV on MgO-Ag(100)) but lowers the activation barrier by 0.28 eV. However, dissociated water is still less stable. The authors were able to use the STM to induce water dissociation via vibrations or excitation into the LUMO. Finally Kawai et al.[91] presented a detailed DFT study of water dissociation on different thicknesses of MgO thin films, in which the thinnest films promoted dissociation by lowering the barrier and stabilising dissociated water.

Song et al examined how supporting MgO (100) on Mo (100) can be used to dissociate water, citing lattice strain as a key factor in promoting water dissociation.[103] They showed that as the MgO lattice expands, from Ag (100) to MgO to Mo (100), the initial adsorption energy of molecular water increases from -0.45 eV to -0.75 eV on MgO-

Mo(100). The dissociative adsorption of water is more favourable on MgO-Mo(100) and is most stable on the thinnest supported MgO film; the adsorption energy is -1.08 eV, compared to -0.67 eV for molecular water adsorption. Finally, computed barriers to water dissociation on thin, supported MgO were less than 0.1 eV.

The interaction of water with CaO has been widely studied as its hydroxylation is key to many properties[93, 104]. In contrast to MgO water dissociates on CaO (100) terraces[94, 100, 105] Experimental results indicated an adsorption energy of water vapour at CaO of 1.5 eV[106]. As part of a study on using the ReaxFF for CaO hydration, Manzano *et al.*[107] undertook DFT calculations of water adsorption on CaO (100). Water dissociates on CaO, with computed energies in the range of -0.96 eV to -1.37 eV, depending on the DFT functional and basis set used. Fujimori *et al.* [108] investigated the interaction of water at CaO (100) films using experiment and DFT studies. From the XPS spectra, evidence for surface hydroxyls was found and hydroxylation of CaO under UHV was effective.

Considering MgO, CaO and BaO (001), Carrasco et al.[100] performed *ab initio* MD simulations of isolated water molecules. The weakest molecular adsorption is at MgO (100), -0.50 eV, while the adsorption energy increases for CaO (-0.80 eV) and BaO (-0.88 eV). The activation barrier on MgO is 1.17 eV, leading to endothermic water dissociation. On CaO the barrier is 0.07 eV and there is no barrier on BaO and water is stable when adsorbed dissociatively on the latter surfaces. This was discussed with respect to the enhanced basicity of CaO and BaO compared to MgO. The AIMD simulations, showed that a “tight ion pair” is formed in which the adsorbed OH can move around the adsorbed H with low barriers.

Groenbeck and Panas[109] presented an *ab initio* molecular dynamics investigate of water on BaO (001). A water coverage of 1/9 ML was used and after less than 1 ps, at an initial temperature of 100 K, water dissociation takes place resulting in the formation of two surface hydroxide (OH^-) groups, which is confirmed from analysis of the electrons density. The adsorption energy of this hydroxide pair is 1.49 eV.

Bajdich et al. [98] presented a detailed study of alkaline earth metal oxides using a range of DFT approaches. In terms of water adsorption, water adsorbed weakly at MgO (100), lying flat and with computed adsorption energies of -0.28 to -0.59 eV for common gradient corrected functionals and HSE; with LDA the adsorption energy is -0.85 eV.

Pfeiffer *et al.* have reviewed the use of alkaline earth oxides for CO_2 capture. The capture of CO_2 occurs chemically through chemisorption and can produce the

corresponding alkaline earth carbonate. These authors showed that MgO and CaO are among the materials with the best CO_2 capture properties, with capacities of 17 mmol/g and 25 mmol/g[87].

In an early study, Pacchioni et al.[97] studied CO_2 adsorption at cluster models of MgO and CaO, using Hartree-Fock and MP2. CO_2 adsorbs at a 5-coordinated oxygen site on both cluster models, with molecular C-O distances of 1.22 and 1.23 Å on MgO and CaO and C-O distance of 1.53 and 1.42 Å to MgO and CaO. On MgO, adsorption at a step site is more stable than on a surface terrace site. The difference between MgO and CaO is proposed to arise from the Madelung potential at surface sites. The smaller Madelung potential on CaO means a more diffuse electron density at the surface and thus better interactions with molecules. Similarly the highest energy occupied states lie at higher energy in CaO than in MgO.

Schneider presented a periodic plane wave DFT study of CO_2 adsorption on the rock salt (100) surface of alkaline earth oxides[101]. He found that CO_2 adsorption was weakest at MgO (100), with a computed adsorption energy of 0.13 eV and CO_2 adsorption becomes more favourable on moving down the alkaline earth group, with significantly larger adsorption energies for CaO, SrO and BaO; the largest change is from MgO to CaO. The preferred adsorption mode is a carbonate-like species with carbon binding to one of the surface oxygen in the (100) terrace. C-O distances in the molecule range from 1.25 (MgO), 1.27 (CaO) and 1.28 Å (BaO), while C-O distances to the surface are 1.47 (MgO), 1.38 (CaO) and 1.36 Å (BaO). The geometry of the adsorbed species tends towards that of a carbonate species on going down the alkaline earth series.

Jensen et al[95] studied CO_2 adsorption on MgO and CaO clusters and focussed on adsorption at terrace versus low coordinated edge sites. Adsorption modes studied included monodentate, on terrace and edge sites, and bidentate/tridentate on edge sites. The most stable adsorption sites on MgO were monodentate on a 4-coordinated oxygen step and tridentate on a 3-coordinate corner oxygen; computed adsorption energies were 1.60 and 1.57 eV. On CaO, the most favourable sites were monodentate on a 4-coordinated oxygen step and monodentate on a 3-coordinate corner oxygen; computed adsorption energies were 2.27 and 2.30 eV.

Downing et al[89] used a QM/MM approach to study CO_2 adsorption at the MgO (100) surface. Two physisorption modes of CO_2 were found: one is perpendicular with one oxygen pointing to the surface terrace and the other lies flat, parallel to the terrace. The flat lying structure had an adsorption energy of -0.046 eV. Chemisorbed CO_2 geometries

were also found. The first is a typical monodentate carbonate with the carbon interacting with a surface oxygen and the O-C-O angle deviates from linearity. The adsorption energy is -0.68 eV and the stability of this adsorption mode was contrasted to earlier work where this was unstable to dissociation into CO and oxygen. A tridentate adsorption mode was found which lies 0.18 eV higher in energy in which the oxygen atoms of CO_2 interact with surface Mg sites. Differences with earlier models were discussed, in particular inclusion of long range polarisation effects in the QM/MM scheme.

A key point about this series of alkaline earth oxides for water and CO_2 adsorption is how their properties change on going down the group. As the ionic radius increases from Mg to Ca to Ba, the Madelung potential of the corresponding oxide decreases. This leads to a more delocalised electron distribution and the oxygen-centred valence band states move to higher energy. This facilitate a stronger interaction with adsorbed molecules, such as water[95, 97] or CO_2 [87, 88, 92, 95, 97, 101, 110] and we will discuss this for our nanocluster-modified rutile systems.

In this paper we use DFT simulations to investigate the surface modification of rutile (110) with alkaline earth oxide nanoclusters. This modification can induce a red shift in light absorption and promote electron and hole separation. Importantly, we show that modification with an MgO nanocluster enhances dissociative adsorption of water, lowering the dissociation barrier when compared to MgO (100). On the other hand, CaO- and BaO-modified rutile result in spontaneous water dissociation to adsorbed surface hydroxyls. Finally, on MgO-rutile CO_2 can adsorb weakly as intact CO_2 or more strongly as a tridentate surface bound carbonate. On CaO-/BaO-rutile, CO_2 adsorbs strongly as a tridentate carbonate. The computed vibrational modes are consistent with carbonate-like adsorption. The adsorption energies of CO_2 on these nanocluster-modified rutile heterostructures, suggest that such structures would be useful for CO_2 capture and storage by CO_2 chemisorption.

Computational Methodology

The TiO_2 rutile (110) surface is studied within a three dimensional periodic slab model and a plane wave basis set that describes the valence electronic wave functions as implemented in the VASP5.3 code[111-113]. The cut-off for the kinetic energy is 396 eV. A comparison of results

with a cut-off energy of 500 eV reveals no changes to the key results of this paper. For example changes in the water and CO_2 adsorption energies are at most 0.06 eV; see Table S1 in the ESI

For the core-valence interaction we apply the projector augmented wave (PAW) method[114, 115]. Ti is described by 4 valence electrons as described in detail in Ref.[116] and oxygen by 6 valence electrons. Of the alkaline earth cations, Mg, Ca and Ba are described with 2, 8 and 10 valence electrons, respectively. Finally, the one electron hydrogen PAW potential is used. Similar to our earlier work, we use the Perdew-Wang91 approximation to the exchange-correlation functional[117]. k-point sampling is performed using the Monkhorst-Pack scheme, with a (2 × 2 × 1) sampling grid.

For describing the 3d electronic states of Ti in TiO_2, we have used the DFT+U approach [9, 12, 84, 118-122]. DFT+U[56, 57] adds a Hubbard U correction to consistently describe reduced metal cation states, such as the Ti^{3+} polaronic states that are found in reduced or photoexcited TiO_2. From the literature, values of U in the range 3 – 5 eV are reasonable[9, 12, 84, 118-122] and, for consistency with our earlier work, we apply U = 4.5 eV to the Ti 3d states throughout this paper. The presence of a valence band hole upon photoexcitation means that the description of the resulting O 2p hole is crucial. Consistent with our earlier work on similar surface modified TiO_2 systems, a +U correction is applied to the O 2p electronic states; the value of U is 5.5 eV[24, 78, 80, 84, 116, 123]. For the alkaline earth metal cations, no +U correction is required, since the electronic states are reasonably well-described with DFT. These DFT+U calculations use robust parameters from the author's own work and the literature which have given consistent descriptions of many TiO_2-based materials and we are primarily interested in how the formation of these composite structures influences the adsorption of molecules, so that the present computational set-up will be reasonable. While we are also interested in electronic properties and how these can be changed by surface modification, we are also cognisant that the current set-up, using a GGA functional with the +U correction will not correctly recover the energy gap of TiO_2 and its modifications. The use of hybrid DFT or a GW approach would remove this limitation. However, with currently available computational resources we cannot apply hybrid DFT within VASP to these surface modified 300 atom systems.

The bulk lattice constants of rutile TiO_2 were computed by fitting a set of constant volume DFT+U energies to a Murnaghan equation of state, giving the following bulk lattice constants: a = b = 4.638 Å, c = 2.973 Å. The rutile (110) surface is constructed

from this bulk and its structure is well known, with two coordinated oxygen (bridging oxygen) terminating the surface. There are 5-fold coordinated Ti and 6-fold coordinated Ti present, with the latter bound to the bridging oxygen and 3-fold-coordinated in-plane oxygen atoms. A (2 × 4) surface supercell is employed; this surface supercell expansion is large enough to allow for adsorption of essentially isolated clusters and has been used in many studies of the rutile (110) surface. The rutile surface slab is 6 O-Ti-O layers thick, with a vacuum gap of 10 Å. The bottom trilayer is held fixed and all other layers are allowed relax. The convergence in the wavefunction relaxation is 0.0001 eV, while the ionic relaxation is converged when the forces on the atoms are less than 0.02 eV/ Å. Fermi level smearing with the Methfessel Paxton scheme is applied, with σ = 0.1 eV. All calculations are spin polarised.

The metal oxide clusters adsorbed at TiO_2, the bare TiO_2 surface and the free metal oxide clusters are calculated in the same periodic supercell, with the same plane wave cut off energy, the same k-point sampling grid and the same PAW potentials, ensuring consistency between calculations. To study cluster adsorption, the MgO, CaO and BaO nanoclusters are first relaxed without a surface present and these relaxed clusters are positioned in a number of configurations at the surface and a full relaxation is performed within the computational set-up described above[124, 125].

The adsorption energy of the nanocluster at the rutile (110) surface is computed from

$$E^{ads} = E((MO)_4\text{-}TiO_2) - [\, E(MO)_4 + E(TiO_2) \,] \quad (1)$$

Where $E((MO)_4\text{-}TiO_2)$ is the total energy of the $(MO)_4$ nanocluster (M = Mg, Ca or Ba) supported on the rutile TiO_2 (110) surface. $E(MO)_4$ and $E(TiO_2)$ are the total energies of the free $(MO)_4$ cluster and the bare surface; a negative adsorption energy signifies that cluster adsorption is stable. In Ref.[92] we showed that aggregation of supported nanoclusters is unfavourable compared to gas phase aggregation, so that once adsorbed the nanoclusters will remain isolated on the surface.

To study adsorption of molecules, we adsorb each molecule individually in different configurations on each oxide nanocluster-TiO_2 composite and compute the adsorption energy relative to the intact free molecule as follows:

$$E^{ads} = E(H_2O@(MO)_4\text{-}TiO_2) - [E((MO)_4\text{-}TiO_2)) + E(H_2O) \,] \quad (2)$$

$$E^{ads} = E(CO_2@(MO)_4\text{-}TiO_2) - [E((MO)_4\text{-}TiO_2)) + E(CO_2) \,] \quad (3)$$

Where Eqn (2) describes water adsorption and Eqn (3) describes CO_2 adsorption.

We model photoexcitation by imposing a triplet electronic state on the system. This promotes an electron to the conduction band, with a corresponding hole in the valence band and enables an evaluation of the energetics and charge localisation associated with photoexcitation. The following energies are computed:

The ground state energy of the composites, $E^{singlet}$.

A single point energy calculation at the ground state geometry with the triplet electronic state, $E^{unrelaxed}$.

Ionic relaxation of the triplet electronic state, $E^{relaxed}$.

From these energies we can compute the singlet-triplet vertical excitation energy as:

$E^{vertical} = E^{unrelaxed}-E^{singlet}$.

This corresponds to the simple VB-CB energy gap from the computed density of states. The singlet-triplet excitation energy is:

$E^{excite}=E^{relaxed}-E^{singlet}$.

This is the difference in energy between the relaxed triplet state and the relaxed singlet state to give an approximation of the excitation energy. Finally, the relaxation (carrier trapping) energy is computed as the difference in the energy between the unrelaxed and relaxed triplet states:

$E^{relax}=E^{unrelaxed}-E^{relaxed}$.

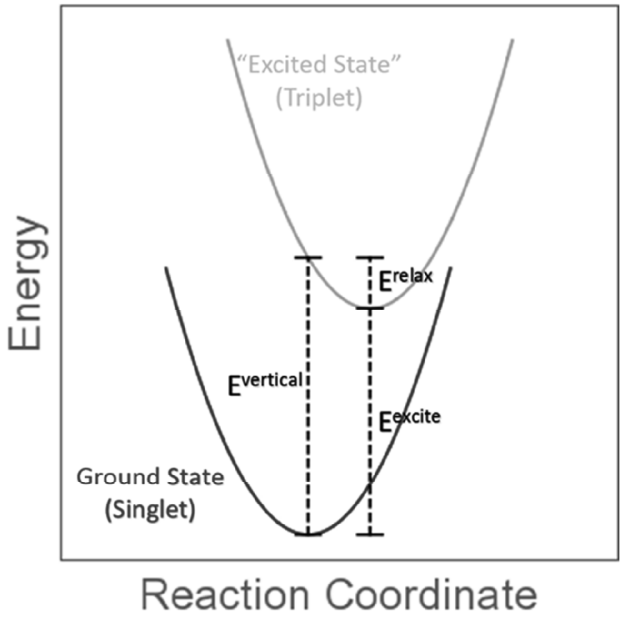


Figure 1. Schematic diagram of the relationship between the energies computed in the photoexcited model.

This is the energy gained when the electron and hole are trapped at their metal and oxygen sites upon structural relaxation and relates to the stability of the trapped electron and hole. These energies are indicated in **Figure 1.**

This model is not intended to replace a full calculation with, e.g. GW or BSE; however neither of these are possible within VASP in our 300 atom supercell models. Being based on our DFT+U set-up it will also suffer from the DFT band gap underestimation. Thus this simple model is not intended to be quantitative but our work has shown that it can, generally, describe red shifts in the energy gap of modified TiO_2 compared to clean surfaces. The most important result of this model is that it allows identification of likely electron and hole localisation sites and trapping energies associated with the stability of localised electrons and holes[126-128].

3. Results

3.1 Alkaline Earth Oxide Nanocluster Modified Rutile (110)

In our previous study[84], we described the structure and properties of MgO-nanocluster modified TiO_2 in detail and in this section we extend this analysis to supported CaO and BaO nanoclusters. The choice of these alkaline earth metal cations also allows the

influence of the cation ionic radius to be analysed as we have previously shown that this can strongly influence, e.g. the dissociation of methane on alkaline earth metal doped CeO_2[129]. We can also examine the impact of the alkaline earth cation on the ability of these composites to adsorb and activated water and CO_2, both of which were the subject of previous studies using extended alkaline earth oxide surfaces[87, 88, 90-92, 95, 97, 98, 100, 101, 130].

We have used the minimum energy DFT relaxed structures of the free $(MO)_4$ alkaline earth oxide nanoclusters and we adsorb these nanoclusters on the dry, perfect rutile (110) surface; a recent study of MgO nanocluster adsorption that compares dry/oxidized and hydroxylated anatase (101) shows that surface hydroxyls have no significant impact on the properties of MgO-TiO_2[120]. As is well known, the adsorption of the nanocluster and the formation of interfacial cluster-surface bonds can strongly modify the structure of the metal oxide nanocluster. For example, the most stable gas phase $(MgO)_4$ cluster is a cube, but upon adsorption at the rutile (110) surface the structure relaxes to be more open; this then allows for the formation of more metal-oxygen interfacial bonds and strengthens the interaction of the cluster with the surface.

The computed adsorption energies of the alkaline earth metal oxide nanoclusters on rutile (110) are: MgO -4.62 eV, CaO -6.77 eV and BaO -6.52 eV and the most stable adsorption structures that we have found are shown in **Figure 2**. The energies indicate that the nanoclusters all adsorb strongly at the rutile (110) surface. Examining Figure 2 we see that the clusters form multiple new interfacial metal-oxygen bonds. In all adsorbed alkaline earth oxide nanoclusters, 8 new cluster-surface bonds are formed.

The adsorption structures in Figure 2 show some common features, but also some dependence on the identity of the alkaline earth metal. All nanoclusters show cluster cations binding to the bridging oxygen of rutile (110). The metal-oxygen distances increase from 1.91 Å for Mg, to 2.21 Å for Ca to 2.54 Å for Ba. These distances are consistent with the increase in ionic radius of the alkaline earth metal cation.

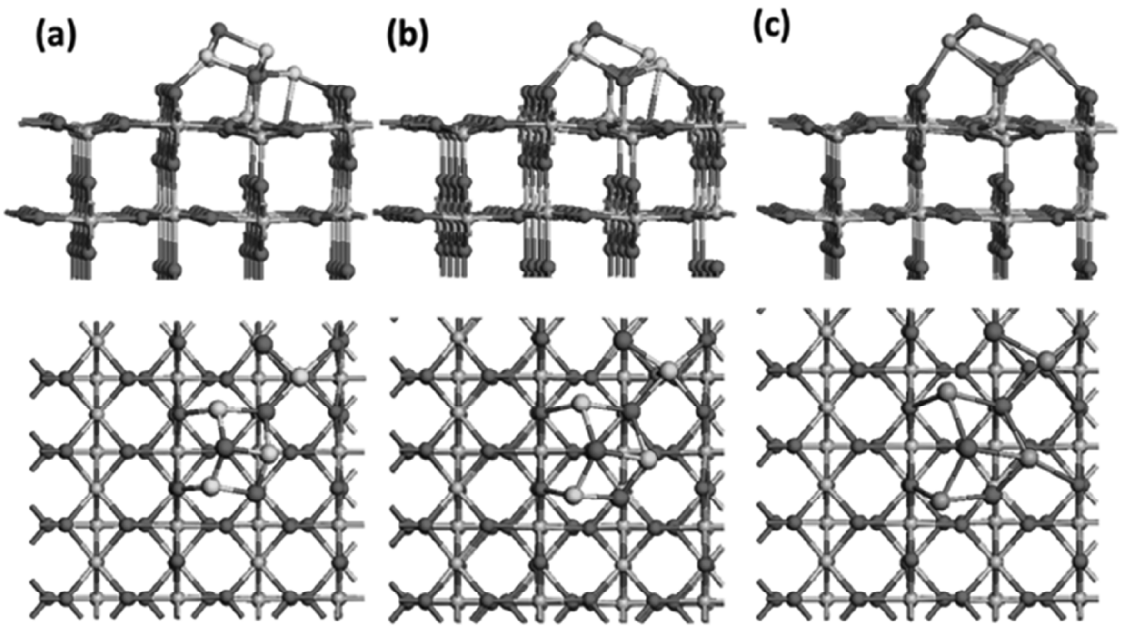


Figure 2: Relaxed atomic structures of alkaline earth oxide nanocluster modified rutile (110) **(a)** $(MgO)_4$, **(b)** $(CaO)_4$, **(c)** $(BaO)_4$. In this and all subsequent figures, Ti atoms are grey spheres, O atoms are red spheres and the alkaline earth metal atoms are green spheres.

$(MgO)_4$ and $(CaO)_4$ both have a metal cation that binds to an in-plane oxygen species, with metal-oxygen distances of 2.15 Å and 2.48 Å for $(MgO)_4$ and $(CaO)_4$. The larger ionic radius of Ba in $(BaO)_4$ prevents formation of this bond; the Ba-O distance is 2.98 Å and instead Ba forms a bond to a bridging 2-coordinated surface oxygen. We can also see that in the surface, Ti cations that bind to oxygen from the nanoclusters migrate out of the surface layer, by *ca.* 0.4 Å as a result of forming this new Ti-O bond. This then elongates the Ti-O bond to the sub surface oxygen in rutile (110).

Figure 3 (a) – (c) shows the Ti 3d and Mg/Ca/Ba *n*s + *n*p and the surface and nanocluster O 2p projected electronic density of states (PEDOS) for the alkaline earth oxide nanocluster modified rutile (110) composites. Examination of the PEODS shows that modification of rutile (110) with $(MgO)_4$ results in formation of O 2p derived cluster states lying at the top of the VB. There are empty Mg-derived states above the conduction band edge of TiO_2. We predict that MgO modification of TiO_2 will lead to little, if any, change to the band gap of TiO_2, with no sizeable shift in light absorption to the visible part of the solar spectrum.

By contrast, for $(CaO)_4$ and $(BaO)_4$ adsorbed at rutile (110), there is a much stronger effect of the nanocluster modification on the valence band region. For both nanoclusters, the nanocluster derived O 2p states lie above the valence band edge of rutile (110), with no modification to the conduction band states. The energy separation of the highest occupied states from the TiO_2 valence band edge is 0.5 eV for $(CaO)_4$-TiO_2 and 0.8 eV for $(BaO)_4$-TiO_2.

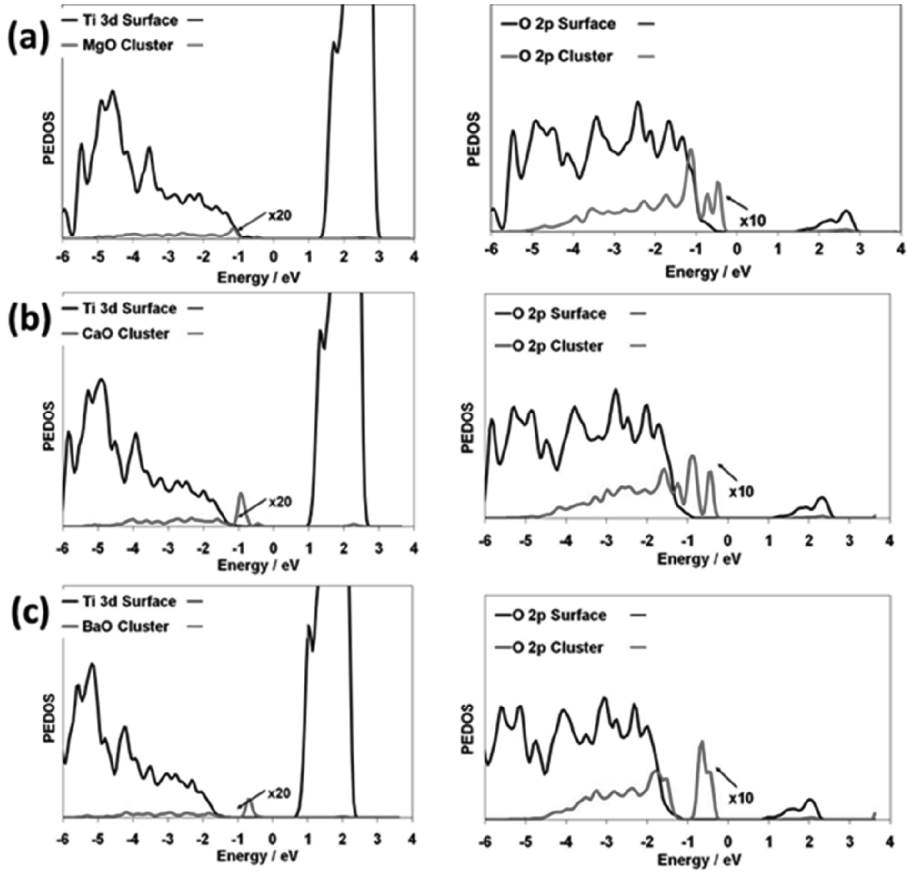


Figure 3: Projected electronic density of states (PEDOS) projected onto Ti 3d and metal *n*s + *n*p states and O 2p states of rutile (110) and the alkaline earth oxide nanoclusters. **(a)** $(MgO)_4$, **(b)** $(CaO)_4$, **(c)** $(BaO)_4$. The PEDOS for the alkaline earth cations and oxygen of the nanoclusters are multiplied by 20 and 10, respectively, to make them visible relative to the TiO_2 surface. In this and all subsequent PEDOS plots, the zero of energy is the Fermi level.

While DFT+U energies are of course not quantitative, we nonetheless can be confident in the qualitative results of a reduction in the energy gap of TiO_2 upon modification. We predict a red shift in light absorption to the visible region upon modification of rutile (110) with CaO and BaO nanoclusters. These findings are consistent with the known characteristics of the corresponding bulk oxides, in which the band gap decreases on going from MgO (6.4 eV)[99] to CaO (5.7 eV)[99] to BaO (4.8 eV)[99] and this is usually explained by the different Madelung potentials in each oxide which determine the position of the highest lying valence band states[97]. This also holds for these supported alkaline earth oxide nanoclusters

To investigate the nature of the photoexcited state and electron and hole localisation and stability, which relate to charge separation after excitation, **Figure 4** displays the excess spin density isosurfaces for the triplet electronic state of each nanocluster modified system. As described in our earlier studies[18, 24, 77, 78, 120, 123] as well as other work[61, 83], this model system allows us to study the nature of the photoexcited state and the charge localisation after excitation. Imposing a triplet electronic state forces an electron into the previously empty conduction band states, leaving a hole in the valence band. Upon relaxation, the electron and hole localise onto atomic sites and this gives a (simple) model of an excited electron-hole pair from which electron and hole localisation can be determined.

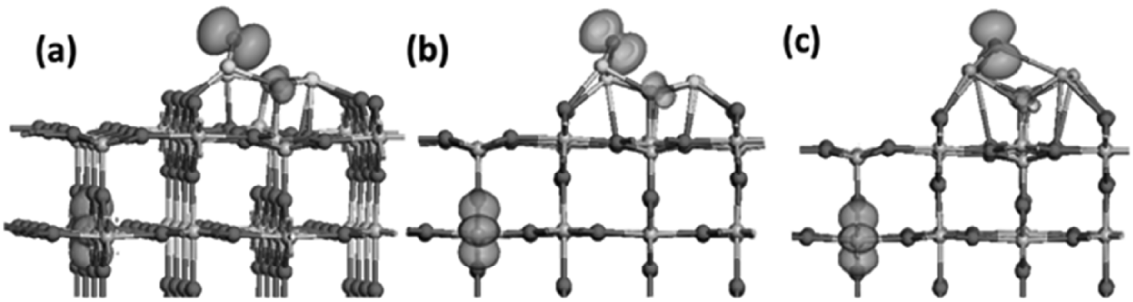


Figure 4: Atomic structures and spin density isosurfaces of alkaline earth oxide nanocluster modified rutile (110) in the triplet electronic state **(a)** $(MgO)_4$, **(b)** $(CaO)_4$, **(c)** $(BaO)_4$. The orange spin density isosurfaces enclose spin densities up to 0.02 electrons/$Å^3$

The spin density isosurfaces in figure 4 show that in all composite structures, the valence band hole localises on an oxygen atom in the nanocluster, forming a an oxygen hole (O^-

, with electronic configuration $2s^2,2p^5$) polaron state. The computed Bader charges for these oxygen sites are 6.9, 6.9 and 6.9 electrons for $(MgO)_4$, $(CaO)_4$ and $(BaO)_4$, while the spin magnetisations are 0.75 μ_B. The computed spin magnetisations on the remaining nanocluster oxygen sites are less than 0.1 μ_B. Typical O^{2-} Bader charges are 7.3 electrons. The formation of the localised oxygen hole state is coupled to an elongation of the cation-O^- bond distance as follows: from 1.90 Å in the $(MgO)_4$-TiO_2 ground state to 2.00 Å in the triplet state, from 2.1/2.29 Å in the $(CaO)_4$-TiO_2 ground state to 2.23/2.36 Å in the triplet state and from 2.42/2.58 Å in the $(BaO)_4$-TiO_2 ground state to 2.71/2.99 Å in the triplet state. The localisation of the oxygen hole also reduces the coordination of this oxygen from 3-fold to 2-fold.

The electron localises onto a subsurface Ti atom in the rutile (110) surface forming a reduced Ti^{3+} species; the computed Bader charge on this Ti in each structure is 1.64 electrons (for Ti^{4+} the computed Bader charge is *ca.* 1.3 electrons), while the corresponding spin magnetisations are 0.95 μ_B. The Ti-O distances elongate to 2.02 – 2.03 Å. Thus, the excitation model predicts electron and hole separation arising from the structure of the composite system and this will reduce charge recombination.

The computed energies for the photoexcited state are given in Table 1. For all heterostructures the vertical excitation energies are red shifted from the 2.21 eV computed for unmodified rutile (110). For $(MgO)_4$-rutile, there is little change in the singlet-triplet energy of 1.69 eV computed for bare rutile (110). For $(CaO)_4$-rutile, the singlet-triplet energy is significantly reduced compared to bare rutile (110). Both results confirm the analysis from the simple PEDOS. We see for $(BaO)_4$-rutile that the singlet-triplet excitation energy is almost 0 eV which most likely arises from the underestimation of the valence to conduction band energy gap as a result of using DFT+U on these systems, as we previously found for PbO_2-modified anatase (001)[81] and this is a limitation of this simple approach. The relaxation energy for (CaO)-rutile is larger than the computed value of 0.52 eV in bare rutile (110), as a result of the great structural flexibility in the nanocluster.

Structure	$E^{vertical}$ / eV	E^{S-T} / eV	E^{Relax} / eV
$(MgO)_4$-rutile	1.98	1.70	0.28
$(CaO)_4$-rutile	1.86	0.93	0.93
$(BaO)_4$-rutile	1.69	0.09	1.60

Table 1: Computed energies for the vertical, singlet-triplet (S-T) and relaxation energies in alkaline earth oxide nanocluster modified rutile (110). These energies correspond to those in Figure 1.

3.2 Adsorption of Water at Alkaline Earth Oxide Modified Rutile (110)

The interaction of water at metal oxides is an important interaction in catalysis. This interaction has been studied on extended alkaline earth oxide surfaces and ultra-thin supported MgO films, as described in the Introduction. In this section we describe our results on the interaction of water at the alkaline earth oxide nanocluster modified rutile (110) composites. We investigate the interaction of one water molecule with an emphasis on the stabilities of molecularly and dissociatively adsorbed water. We recall, that at the extended (100) surfaces of MgO, CaO and BaO water prefers to adsorb (weakly) molecularly on MgO (100) and dissociatively on CaO and BaO (100)

Figures 5 and 6 show the relaxed absorption structures after relaxation of one water molecule adsorbed on $(MgO)_4$-rutile (**figure 5**) and $(CaO)_4$-/$(BaO)_4$-rutile (**figure 6**). On all structures, water was initially adsorbed in molecular and dissociative configurations and then allowed to relax. The computed adsorption energies for the most stable relaxed adsorption structures for each water adsorption mode are given in **Table 2**.

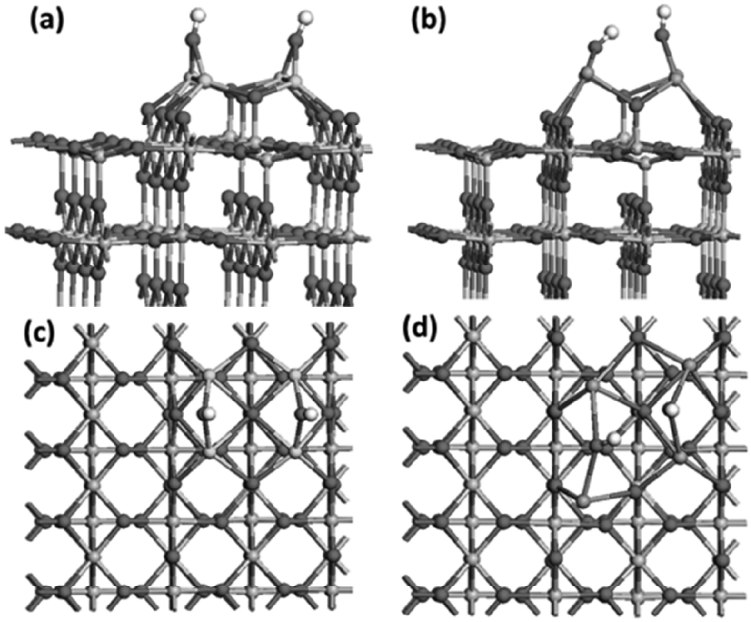


Figure 5: Relaxed atomic structures after **(a), (c)** molecular water adsorption on $(MgO)_4$-modified rutile (110) and **(b), (d)** dissociative water adsorption on $(MgO)_4$-modified rutile (110). The colour coding is the same as figure 1, except that hydrogen is represented by white spheres

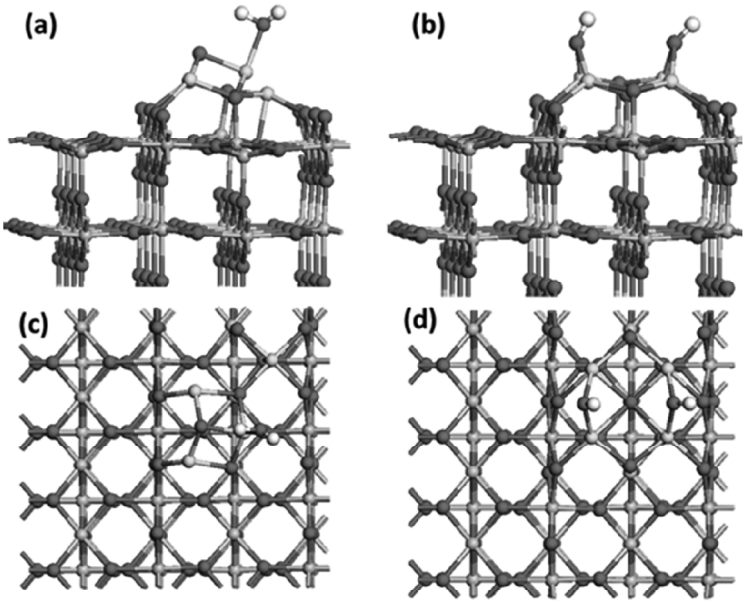


Figure 6: Relaxed atomic structures after water adsorption and relaxation at **(a), (c)** $(CaO)_4$-modified rutile (110) and **(b), (d)** $(BaO)_4$-modified rutile (110). Molecular adsorption of water relaxes to dissociative water adsorption. The colour coding is the same as Figure 5

Molecular Water Adsorption	
Structure	**E^{ads} / eV**
$(MgO)_4$-rutile	-1.28
$(CaO)_4$-rutile	--
$(BaO)_4$-rutile	--
Dissociative Water Adsorption	
Structure	E^{ads} / eV
$(MgO)_4$-rutile	-3.27
$(CaO)_4$-rutile	-3.68
$(BaO)_4$-rutile	-2.58

Table 2: Computed adsorption energies of water (E^{ads}) at the alkaline earth metal oxide nanocluster-modified rutile (110) composites. For $(CaO)_4$- and $(BaO)_4$-rutile, molecular water adsorption relaxes to dissociated water.

On $(MgO)_4$-TiO_2, dissociative adsorption of water is more stable than molecular adsorption by 1.99 eV. Using climbing image nudged elastic band (CI-NEB)[131, 132] we used three images to estimate the barrier to water dissociation on $(MgO)_4$-rutile (110). The computed barrier is 0.36 eV and the transition state is shown in Figure S1 of the ESI. In this TS the two O-H bonds are forming, with O-H distances of 1.09 and 0.97 Å. We can compare this barrier to that computed on other metal oxides such as MgO, CeO_2 or TiO_2. On CeO_2 (111) the computed barrier ranges from 0.14 eV to 0.19 eV to 0.20 eV [133-136]. On rutile (110), the computed barrier depends on the coverage and can range from 0.25 eV – 0.45 eV (from high to low coverage)[137], while the study in ref.[138] found barriers from 0.14 – 0.16 eV. Finally, in ref[139] computed barriers of 0.19 – 0.27 eV were found and strain in the (110) surface lowered the barrier. As discussed in the introduction, the computed barrier for water dissociation on extended MgO (100) is 1.09 eV[91]. Thus, the modification of rutile (110) with $(MgO)_4$ gives a barrier for water dissociation that is at least competitive with TiO_2 or CeO_2 and significantly reduced over bare MgO (100), so that water dissociation will be more likely on $(MgO)_4$-rutile (110), which may promote the water oxidation half reaction in water splitting. The enhanced activity of this heterostructure compared to MgO arises from the presence of the low coordinated and active atomic sites in supported $(MgO)_4$.

On $(CaO)_4$- and $(BaO)_4$-modified rutile (110) when water is initially adsorbed molecularly, it spontaneously dissociates upon relaxation, with no barrier and this results in two hydroxyl species bound on the corresponding nanocluster. Similar findings are reported on the corresponding extended CaO and BaO (100) surfaces[94,100,106,107,109] The energy gain here is significant, with computed adsorption energies of -3.68 and -2.58 eV on $(CaO)_4$- and $(BaO)_4$-rutile. Thus the modification of rutile TiO_2 with the larger ionic radius alkaline earth metal oxide nanoclusters appears to provide active sites that promote direct dissociation of water, in addition to the high lying O 2p states from the alkaline earth oxide. We have been unable to find an adsorption structure of water in its molecular form. This is a significant result as the dissociation of water is a key step in a number of critical catalytic reactions, such as water gas shift[12, 140, 141]. However, we note that the large adsorption energy of hydroxyls on $(MgO)_4$- and $(CaO)_4$-rutile (110) suggests that these heterostructures will be easily hydroxylated and the hydroxyls may show high stability.

Examining the characteristics of adsorbed water, on $(MgO)_4$-TiO_2, molecular water has an Mg-O distance of 2.03 Å, typical for adsorption of intact water. This Mg cation was originally 3-fold coordinated and after interaction with oxygen in water is now 4-fold coordinated.

Upon formation of the two surface hydroxyls the structures around the hydroxyl adsorption sites undergo similar changes on each composite. The four metal cations take a square structure in which each newly formed hydroxyl bridges two cations, with symmetric cation-hydroxyl distances of 1.99 Å (x2), 2.23/2.40 Å for $(MgO)_4$-TiO_2 and $(CaO)_4TiO_2$. On $(BaO)_4$-TiO_2 the large ionic radius of Ba means that the local atomic structure around the cations is more distorted, with Ba-O distances of 2.50, 2.51, 2.57 and 2.71 Å to the hydroxyls. Within the nanoclusters, the Mg-O, Ca-O and Ba-O distances are 2.01 – 2.15 Å, 2.27 – 2.48 Å and 2.49 – 2.79 Å, respectively. The binding of the metal cations to the hydroxyls elongates the metal-oxygen bonds involving surface oxygen by up to 0.2 Å.

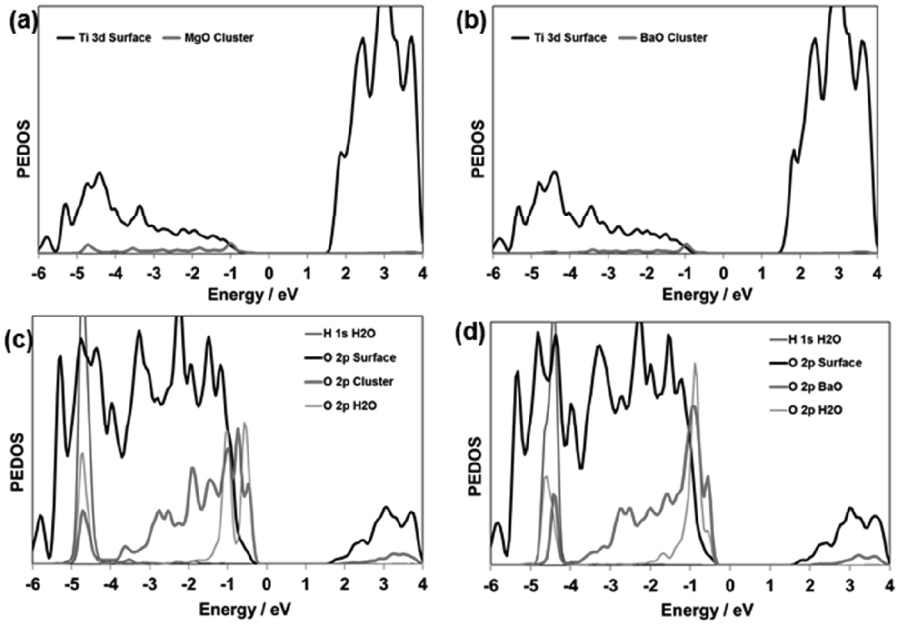


Figure 7: PEDOS after water adsorption at (MgO)4-modified rutile (110) **(a), (c)** molecular water adsorption **(b), (d)** dissociative water adsorption

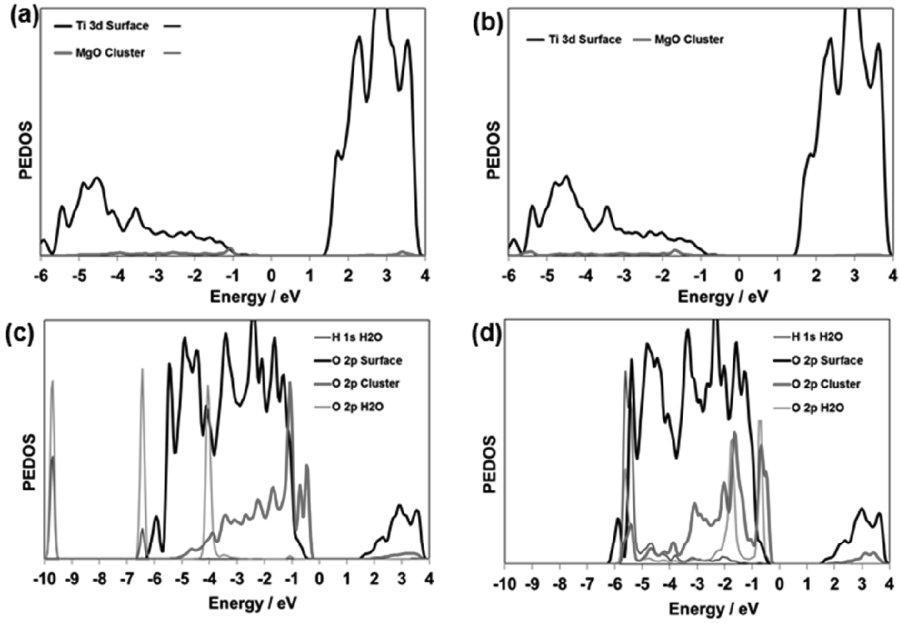


Figure 8: PEDOS after dissociative water adsorption at **(a), (c)** $(CaO)_4$-modified rutile (110) **(b), (d)** $(BaO)_4$-modified rutile (110)

Figure 7 shows the PEDOS for water adsorbed molecularly and dissociatively at the $(MgO)_4$-rutile (110) composite and **Figure 8** shows the PEDOS for dissociative

adsorption of water at the $(CaO)_4$-/$(BaO)_4$-rutile (110) composites. Considering first water adsorption at the $(MgO)_4$-rutile composites, there are clear differences in the PEDOS for molecular and dissociative water adsorption. Molecular water shows sharp, localised water derived O 2p peaks which lie at 4 eV, 6.5 eV and 10 eV below the valance band edge. After dissociation, these peaks shift to higher energies and the strong interaction between water and $(MgO)_4$ results in water derived O 2p peaks at the top of the valance band and at 2 eV below the valence band edge.

For the $(CaO)_4$- and $(BaO)_4$-TiO_2 structures, the adsorption of water as hydroxyls results in the appearance of water derived O 2p states at the top of the valance band; this is most apparent for $(CaO)_4$ and these PEDOS peaks are rather broad. We note that the presence of adsorbed water results in a shift of the previously high lying nanocluster derived O 2p states towards the TiO_2 valance band region, as these oxygen species are passivated by interaction with hydrogen and thus show increased coordination.

We can attribute the enhancement in dissociative water adsorption and the differences between MgO and CaO/CaO to the non-bulk-like atomic structure of the supported nanoclusters which provide atomic sites favourable for water adsorption. In addition, the higher O 2p derived energy states from CaO and BaO, as a result of the different electrostatic potentials in the alkaline earth metal, means that these states are available to interact with water and this drives the dissociative adsorption of the water molecule.

3.3 Chemisorption and Capture of CO_2 at Alkaline Earth Oxide Modified Rutile (110)

As discussed in the literature the alkaline earth oxides show some ability to adsorb CO_2, in particular on MgO and CaO and the presence of low coordinated sites can further enhance CO_2 adsorption [21, 88, 92, 95, 97, 130, 142]. In this section we investigate the adsorption of CO_2 at the alkaline earth oxide nanocluster modified TiO_2 heterostructures. **Figure 9** shows the relaxed atomic structures for CO_2 adsorbed at the supported alkaline earth oxide nanoclusters.

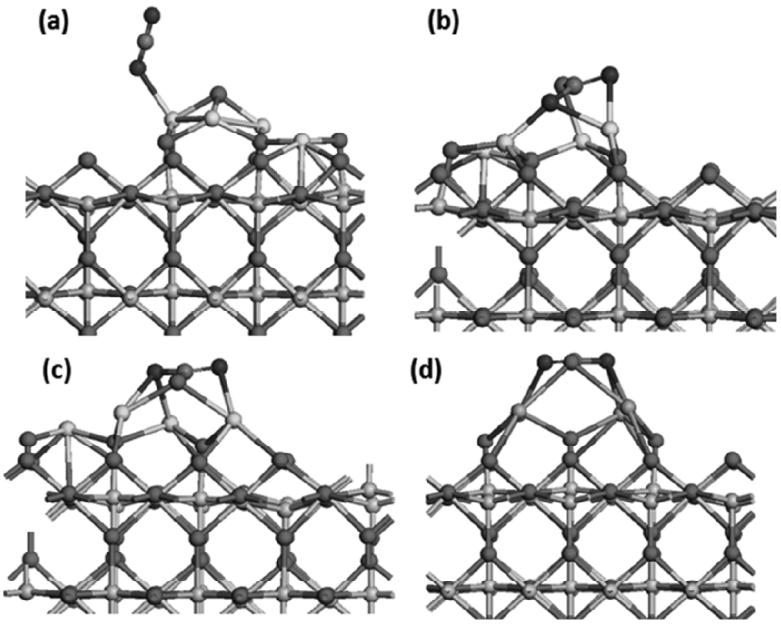


Figure 9: Atomic structures of CO_2 adsorbed at alkaline earth oxide nanocluster modified rutile (110) **(a)** Linear CO_2 adsorption on $(MgO)_4$-rutile, **(b)** CO_2 adsorption as carbonate on $(MgO)_4$-rutile, **(c)**: CO_2 adsorption as carbonate on $(CaO)_4$-rutile, **(d)** CO_2 adsorption as carbonate on $(BaO)_4$-rutile. In this figure, the colour coding is the same as figure 1, with carbon indicated by the grey sphere and oxygen from CO_2 indicated as purple spheres in parts (a), (b), (c) and (d).

On $(MgO)_4$-rutile, we found two CO_2 adsorption modes that are exothermic. The first mode is shown in figure 9 (a) and in this mode an oxygen atom from CO_2 interacts with one of the Mg atoms in the nanocluster. The resulting adsorption energy is -0.64 eV which although larger than on many stoichiometric metal oxides can still be considered weak; if we consider the entropy of gas phase CO_2 at 298 K, which is 0.66 eV, then CO_2 would not be expected to bind strongly in this adsorption mode. The Mg-O distance to CO_2 is 2.17 Å, slightly longer than a typical Mg-O distance and CO_2 remains linear (even when relaxed starting from a bent O-C-O configuration), with computed C=O distances of 1.19 and 1.16 Å. The slightly longer C=O distance involves the oxygen atom bound to Mg in the nanocluster. Loss of CO from this structure is computed to be highly endothermic, with an energy cost of 4.18 eV.

The second and most stable adsorption mode is shown in figure 9 (b) with a computed adsorption energy of -2.24 eV, indicating a very strong interaction between CO_2 and $(MgO)_4$-rutile. In adsorbed CO_2, the C-O distances are elongated to 1.29 Å. The carbon atom further binds to an oxygen from the nanocluster, which has migrated to form this

bond, and has a C-O distance of 1.35 Å. This geometry is close to that of an adsorbed carbonate (which would have three equal C-O distances of 1.28 Å) so we can conclude that the most stable adsorption mode of CO_2 is as a bound carbonate. In this adsorption mode, one of the oxygen atoms of CO_2 binds to two Mg cations in the nanocluster, while the other oxygen atom binds to a single Mg cation. The third oxygen in the carbonate bridges carbon and an Mg cation. This is different to the usual carbonate-like binding modes discussed in the literature but it can be described as a *tridentate carbonate* adsorption mode, similar to the tridentate adsorption mode described for CO_2 adsorption at a 3-coordinated corner site[95]. The significantly enhanced adsorption energy compared to rock salt (001) terraces or even step/edge sites previously studied[95, 97, 142] originates from the flexibility in the supported $(MgO)_4$ nanocluster to relax in response to adsorption of the CO_2 molecule.

Figure 9 (c) and (d) show the atomic structure for CO_2 adsorbed at the $(CaO)_4$-rutile and $(BaO)_4$-rutile composites and these are the only stable adsorption modes that we found for CO_2 adsorption at these alkaline earth oxide nanoclusters. The computed absorption energies for CO_2 are -3.99 eV on $(CaO)_4$-rutile and -3.45 eV on $(BaO)_4$-rutile and CO_2 adsorbs in a tridentate configuration. These energies indicate very strong interactions between CO_2 and the supported alkaline earth nanoclusters.

Structure	**CO_2 vibrational modes / cm^{-1}**
$(MgO)_4$-rutile (upright)	2369, 1323, 618, 600
$(MgO)_4$-rutile (carbonate)	1489, 1276, 1016, 844
$(CaO)_4$-rutile	1439, 1345, 1034, 816
$(BaO)_4$-rutile	1382, 1356, 1020, 823

Table 3: Computed CO_2 vibrational modes after adsorption on $(MgO)_4$-rutile (with two adsorption modes: upright Figure 9(a) and carbonate, Figure 9(b)), $(CaO)_4$-rutile and $(BaO)_4$-rutile. The modes for gas phase CO_2 are 2349 (asymmetric C=O stretch), 1388 (symmetric C=O stretch) and 667 cm^{-1} (C=O bending, degenerate)

We have computed the vibrational modes of adsorbed CO_2 in each case and these are given in **table 3**. The vibrational modes of weakly adsorbed CO_2 on $(MgO)_4$-rutile are little changed from the free CO_2 molecule as expected from the weak interaction and

unmodified CO_2 geometry. On the other hand when CO_2 adsorbs strongly on all three alkaline earth oxide modified rutile systems, the significant red shift in the asymmetric C=O stretching mode, which is characteristic of CO_2 distortion, is clearly present, which agrees with experimental and theoretical studies for strong CO_2 adsorption. The adsorption in this way also breaks the degeneracy of the C=O bending modes.

The C-O distances in the adsorbed CO_2 molecule are 1.29, and 1.30 Å in $(CaO)_4$-rutile and 1.29 and 1.30 Å in $(BaO)_4$-rutile. The C-O distance to oxygen in the nanocluster is 1.32 Å in $(CaO)_4$-rutile and 1.31 Å in $(BaO)_4$-rutile. Thus CO_2 adsorbs strongly on $(CaO)_4$ and $(BaO)_4$ and displays a typical carbonate geometry.

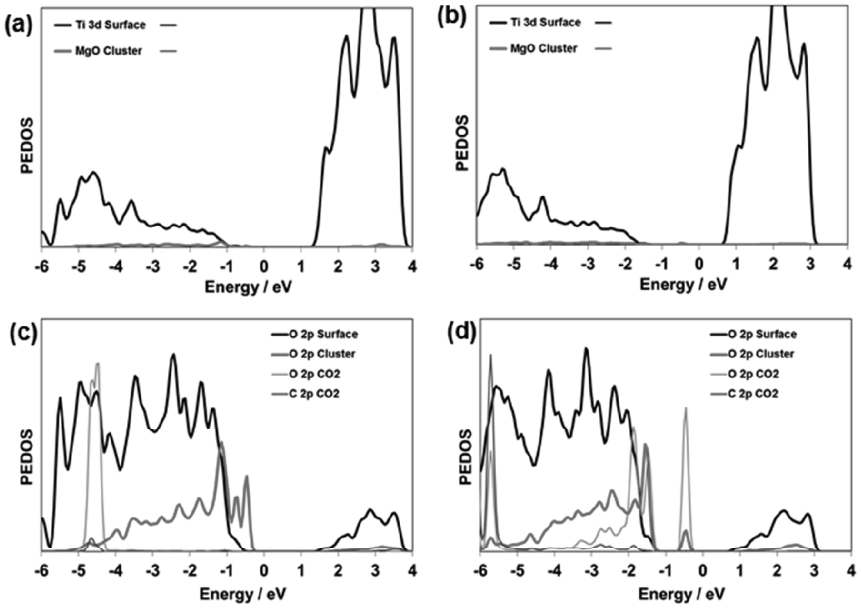


Figure 10: PEDOS after CO_2 adsorption on MgO-rutile (110) **(a), (c):** linear CO_2 and **(b), (d):** carbonate-like adsorption mode

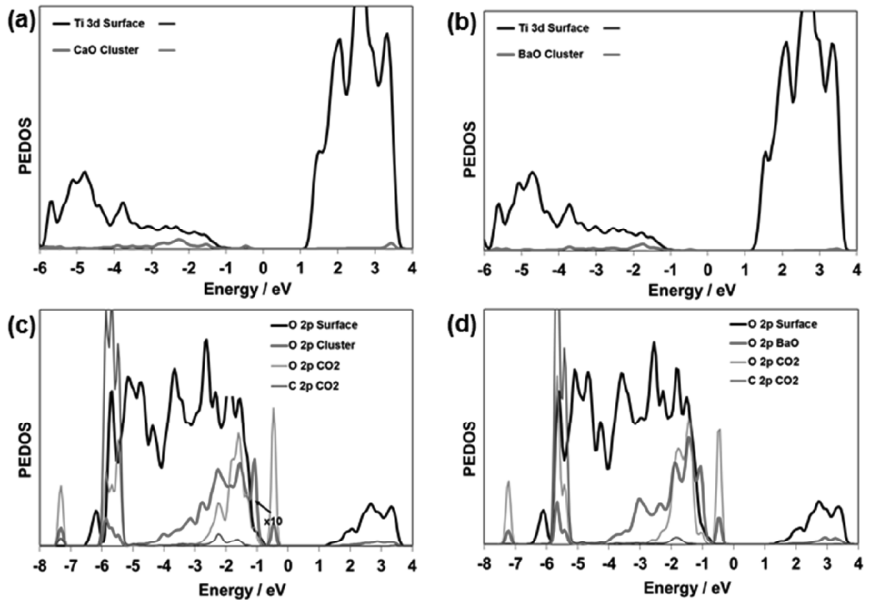


Figure 11: PEDOS after CO_2 adsorption on **(a, (c)):** $(CaO)_4$-rutile (110) and **(b), (d):** $(BaO)_4$-rutile (110)

Figure 10 and **figure 11** show the computed PEDOS for CO_2 adsorption at $(MgO)_4$-rutile and $(CaO)_4$-/$(BaO)_4$-rutile. On $(MgO)_4$-rutile, the PEDOS of CO_2 in the two adsorption modes are clearly different, reflecting the nature of each adsorption mode. In the upright adsorption mode, the CO_2 derived C 2p and O 2p peaks lie 4.5 eV below the valence band edge of the oxide and display a narrow peak. By contrast, when CO_2 adsorbs as a carbonate, there is a strong CO_2-derived PEDOS peak in the energy gap of $(MgO)_4$-rutile and a second, broad PEDOS peak that lies at the top of the valance band, which is characteristic of a strong interaction between CO_2 and the oxide heterostructure.

The stronger adsorption of CO_2 at $(CaO)_4$ and $(BaO)_4$ can be understood when comparing their properties to $(MgO)_4$. Particularly important is that the highest occupied electronic states in $(CaO)_4$ and $(BaO)_4$ lie at higher energy above the TiO_2 VB edge compared to $(MgO)_4$ and their increased basicity, as discussed in ref. [97]. This then facilitates a stronger interaction between the supported metal oxide nanocluster and CO_2.

Finally, we have applied the model of the triplet electronic state to CO_2 bound in the carbonate adsorption mode and the atomic structure and spin density are shown in Figure S2 of the ESI. In the triplet state of CO_2 adsorbed on $(CaO)_4$-rutile and $(BaO)_4$-

rutile the hole localises over carbon atoms of the carbonate, while the electron localises on a sub-surface Ti atom in the rutile (110) surface. On $(MgO)_4$-rutile, the hole localises onto an oxygen atom of the nanocluster.

While such strong adsorption energies and carbonate formation clearly preclude these systems from being useful in conversion of CO_2, they may be useful for the capture and storage of CO_2, under the assumption that the CO_2 so absorbed is not going to be used as a feedstock. The latter requires CO_2 physisorption so as to allow the CO_2 to be released for chemical conversion. The strong interactions, particularly at $(CaO)_4$-rutile mean that the carbonate so formed will not be easily removed and should remain bound to the $(CaO)_4$-rutile composite. Thus, these composites could be interesting and inexpensive materials to explore for chemisorption-based carbon capture where the captured CO_2 is to be stored rather than re-used.

4. Conclusions

We have presented a first principles density functional theory (DFT) study of the modification of rutile TiO_2 (110) with nanoclusters of the alkaline earth metal oxides (MgO, Ca, BaO). We have focussed on the effect of surface modification on key catalyst properties including stability, light absorption, charge localisation and activity towards H_2O and CO_2.

The modification of rutile TiO_2 with alkaline earth oxide nanoclusters can induce a red shift in light absorption with CaO and BaO. In all cases, photoexcited electrons and holes separate and localise on low-coordinated oxygen in the nanocluster and sub-surface Ti sites, thus enhancing charge separation.

The presence of these non-bulk alkaline earth oxide nanoclusters provides highly active sites for water and CO_2 adsorption. On MgO-rutile, water adsorbs molecularly and the barrier to dissociation is only 0.36 eV, which is a significant reduction over extended MgO (100). On CaO- and BaO-rutile water adsorbs dissociatively upon relaxation. We attribute this result to the high lying O 2p states in the alkaline earth oxide modifiers which are available to interact with water, as well as the non-bulk like geometry around the active site.

Finally, upon adsorption of CO_2 the preferred binding mode is a tridentate species, which becomes more carbonate-like on going from MgO to CaO to BaO, as

characterised by geometry and computed vibrational modes. This carbonate is bound by up to 4 eV. This makes these heterostructures interesting for CO_2 capture, thus helping alleviate the problem of CO_2 emissions.

Conflict of Interest

There are no conflicts of interest to declare

Acknowledgements

We acknowledge support from the Science Foundation Ireland funded US-Ireland R&D Partnership Program project SusChem grant: SFI 14/US/E2915, the SFI-funded The H2020 supported M-ERANET-2 2016 project RATOCAT (H2020 Grant Number 685451 and SFI Grant Number 16/M-ERA/3418). The PRACE-DECI program (Grants RI-312763 and 653838), the SFI/HEA funded Irish Centre for High-end Computing (ICHEC) and SFI funded local computing clusters at Tyndall are acknowledged for generous access to computing resources. The COST ACTION CM1104 is also thanked for support.

References:

1. A. Fujishima, X. Zhang and D. A. Tryk, *Surf. Sci. Rep.*, 2008, 63, 515-582.
2. C. Jiang, S. J. A. Moniz, A. Wang, T. Zhang and J. Tang, *Chem. Soc. Rev.*, 2017, 46, 4645-4660.
3. K. Maeda and K. Domen, *J. Phys. Chem. Lett.*, 2010, 1, 2655-2661.
4. M. Ni, M. K. H. Leung, D. Y. C. Leung and K. Sumathy, *Renew. Sustainable Energy Rev.*, 2007, 11, 401-425.
5. L. I. Bendavid and E. A. Carter, *J. Phys. Chem. C*, 2013, 117, 26048-26059.
6. X. Chang, T. Wang and J. Gong, *Energy Environ Sci.*, 2016, 9, 2177-2196.
7. N. M. Dimitrijevic, B. K. Vijayan, O. G. Poluektov, T. Rajh, K. A. Gray, H. He and P. Zapol, *J. Am. Chem. Soc.*, 2011, 133, 3964-3971.
8. W. J. Durand, A. A. Peterson, F. Studt, F. Abild-Pedersen and J. K. Nørskov, *Surf. Sci.*, 2011, 605, 1354-1359.
9. M. Fronzi, W. Daly and M. Nolan, *Applied Catalysis A:* , 2016, 521, 240-249.
10. A. Goeppert, M. Czaun, J.-P. Jones, G. K. Surya Prakash and G. A. Olah, *Chem. Soc. Rev.*, 2014, 43, 7995-8048.

11. L. C. Grabow and M. Mavrikakis, *ACS Catal.*, 2011, 1, 365-384.
12. J. Graciani, K. Mudiyanselage, F. Xu, A. E. Baber, J. Evans, S. D. Senanayake, D. J. Stacchiola, P. Liu, J. Hrbek, J. F. Sanz and J. A. Rodriguez, *Science*, 2014, 345, 546-550.
13. S. N. Habisreutinger, L. Schmidt-Mende and J. K. Stolarczyk, *Angew. Chem. Int. Ed.*, 2013, 52, 7372-7408.
14. D. Jiang, W. Wang, E. Gao, S. Sun and L. Zhang, *Chem. Commun.*, 2014, 50, 2005-2007.
15. L. Liu, C. Zhao and Y. Li, *J. Phys. Chem. C*, 2012, 116, 7904-7912.
16. A. K. Mishra, A. Roldan and N. H. de Leeuw, *J. Phys. Chem. C*, 2016, 120, 2198-2214.
17. S. C. Roy, O. K. Varghese, M. Paulose and C. A. Grimes, *ACS Nano*, 2010, 4, 1259-1278.
18. K. C. Schwartzenberg, J. W. J. Hamilton, A. K. Lucid, E. Weitz, J. Notestein, M. Nolan, J. A. Byrne and K. A. Gray, *Catal. Today*, 2017, 280, 65-73.
19. C. Song, *Global Challenges and Strategies for Control, Conversion and Utilization of CO2 for Sustainable Development Involving Energy, Catalysis, Adsorption and Chemical Processing*, 2006.
20. E. L. Uzunova, N. Seriani and H. Mikosch, *Phys. Chem. Chem. Phys.*, 2015, 17, 11088-11094.
21. S. Xie, Y. Wang, Q. Zhang, W. Deng and Y. Wang, *ACS Catal.*, 2014, 4, 3644-3653.
22. M. Pelaez, N. T. Nolan, S. C. Pillai, M. K. Seery, P. Falaras, A. G. Kontos, P. S. M. Dunlop, J. W. J. Hamilton, J. A. Byrne, K. O'Shea, M. H. Entezari and D. D. Dionysiou, *Appl. Catal., B*, 2012, 125, 331-349.
23. V. Etacheri, C. Di Valentin, J. Schneider, D. Bahnemann and S. C. Pillai, *J. Photochem. Photobiol. C: Photochem. Rev.*, 2015, 25, 1-29.
24. H. Tada, Q. Jin, A. Iwaszuk and M. Nolan, *J. Phys. Chem. C*, 2014, 118, 12077-12086.
25. L. Bian, M. Song, T. Zhou, X. Zhao and Q. Dai, *J. Rare Earths*, 2009, 27, 461-468.
26. R. Chand, E. Obuchi, K. Katoh, H. N. Luitel and K. Nakano, *Catal. Commun.*, 2011, 13, 49-53.

27. B. Choudhury, M. Dey and A. Choudhury, *International Nano Letters*, 2013, 3, 1-8.
28. G. Colón, M. Maicu, M. C. Hidalgo and J. A. Navío, *Appl. Catal., B*, 2006, 67, 41-51.
29. Y. Cui, H. Du and L. Wen, *J. Mater. Sci. Technol.*, 2008, 24, 675-689.
30. A. M. Czoska, S. Livraghi, M. Chiesa, E. Giamello, S. Agnoli, G. Granozzi, E. Finazzi, C. D. Valentin and G. Pacchioni, *J. Phys. Chem. C*, 2008, 112, 8951-8956.
31. C. Di Valentin, E. Finazzi, G. Pacchioni, A. Selloni, S. Livraghi, M. C. Paganini and E. Giamello, *Chem. Phys.*, 2007, 339, 44-56.
32. Y. Gai, J. Li, S. S. Li, J. B. Xia and S. H. Wei, *Phys. Rev. Lett.*, 2009, 102, 036402.
33. M. Guo and J. Du, *Physica B: Condensed Matter*, 2012, 407, 1003-1007.
34. P. Haowei, L. Jingbo, L. Shu-Shen and X. Jian-Bai, *J. Phys.: Condens. Matter*, 2008, 20, 125207.
35. J.-M. Herrmann, *New J. Chem.*, 2012, 36, 883-890.
36. T. Ikeda, T. Nomoto, K. Eda, Y. Mizutani, H. Kato, A. Kudo and H. Onishi, *J. Phys. Chem. C*, 2008, 112, 1167-1173.
37. A. Iwaszuk and M. Nolan, *J. Phys.: Condens. Matter*, 2011, 23, 334207.
38. A. Iwaszuk and M. Nolan, *J. Phys. Chem. C*, 2011, 115, 12995-13007.
39. C. Karunakaran, G. Abiramasundari, P. Gomathisankar, G. Manikandan and V. Anandi, *J. Colloid Interface Sci.*, 2010, 352, 68-74.
40. R. Long and N. J. English, *J. Phys. Chem. C*, 2010, 114, 11984-11990.
41. S. Na Phattalung, S. Limpijumnong and J. Yu, *Appl. Catal., B*, 2017, 200, 1-9.
42. J. Navas, A. Sánchez-Coronilla, T. Aguilar, N. C. Hernández, M. Desireé, J. Sánchez-Márquez, D. Zorrilla, C. Fernández-Lorenzo, R. Alcántara and J. Martín-Calleja, *Phys. Chem. Chem. Phys.*, 2014, 16, 3835-3845.
43. X. Nie, S. Zhuo, G. Maeng and K. Sohlberg, *Int. J. Photoenergy*, 2009, 2009, 22.
44. C. D. Valentin, G. Pacchioni, H. Onishi and A. Kudo, *Chem. Phys. Lett.*, 2009, 469, 166-171.
45. Y. Wang, R. Zhang, J. Li, L. Li and S. Lin, *Nanoscale research letters*, 2014, 9, 1.
46. J.-P. Xu, L. Li, L.-Y. Lv, X.-S. Zhang, X.-M. Chen, J.-F. Wang, F.-M. Zhang, W. Zhong and Y.-W. Du, *Chin. Phys. Lett.*, 2009, 26, 097502.

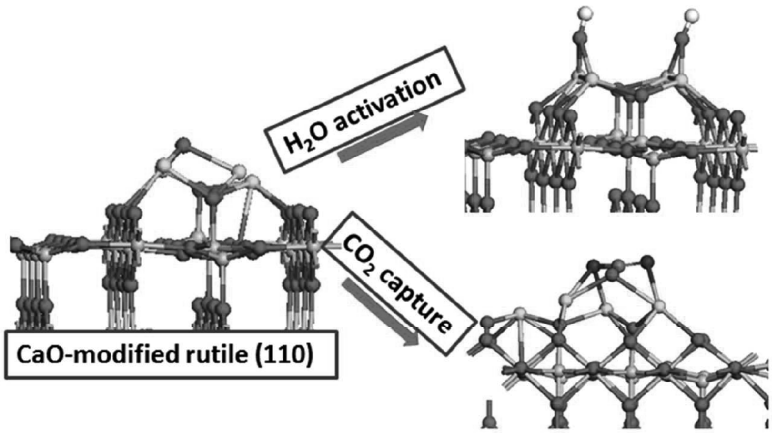
47. K. Yang, Y. Dai and B. Huang, *J. Phys. Chem. C*, 2007, 111, 12086-12090.
48. K. Yang, Y. Dai, B. Huang and M.-H. Whangbo, *J. Phys. Chem. C*, 2009, 113, 2624-2629.
49. L. S. Yoong, F. K. Chong and B. K. Dutta, *Energy*, 2009, 34, 1652-1661.
50. H. Zhang, X. Yu, J. A. McLeod and X. Sun, *Chem. Phys. Lett.*, 2014, 612, 106-110.
51. J. Zhang, C. Pan, P. Fang, J. Wei and R. Xiong, *ACS Appl. Mater. Interfaces*, 2010, 2, 1173-1176.
52. J. W. Zheng, A. Bhattcahrayya, P. Wu, Z. Chen, J. Highfield, Z. Dong and R. Xu, *J. Phys. Chem. C*, 2010, 114, 7063-7069.
53. W. Zhu, X. Qiu, V. Iancu, X.-Q. Chen, H. Pan, W. Wang, N. M. Dimitrijevic, T. Rajh, H. M. Meyer, M. P. Paranthaman, G. M. Stocks, H. H. Weitering, B. Gu, G. Eres and Z. Zhang, *Phys. Rev. Lett.*, 2009, 103, 226401.
54. R. Long and N. J. English, *Chem. Mater.*, 2010, 22, 1616-1623.
55. R. Erdogan, O. Ozbek and I. Onal, *Surf. Sci.*, 2010, 604, 1029-1033.
56. F. Xiong, L.-L. Yin, Z. Wang, Y. Jin, G. Sun, X.-Q. Gong and W. Huang, *J. Phys. Chem. C*, 2017, 121, 9991-9999.
57. E. Escamilla-Roa, V. Timón and A. Hernández-Laguna, *Computational and Theoretical Chemistry*, 2012, 981, 59-67.
58. M. Calatayud and C. Minot, *Surf. Sci.*, 2004, 552, 169-179.
59. M. Lazzeri and A. Selloni, *Phys. Rev. Lett.*, 2001, 87, 266105.
60. H. G. Yang, C. H. Sun, S. Z. Qiao, J. Zou, G. Liu, S. C. Smith, H. M. Cheng and G. Q. Lu, *Nature*, 2008, 453, 638.
61. S. K. Wallace and K. P. McKenna, *J. Phys. Chem. C*, 2015, 119, 1913-1920.
62. S. J. A. Moniz, S. A. Shevlin, X. An, Z.-X. Guo and J. Tang, *Chem. Eur. J.*, 2014, 20, 15571-15579.
63. T. R. Gordon, M. Cargnello, T. Paik, F. Mangolini, R. T. Weber, P. Fornasiero and C. B. Murray, *J. Am. Chem. Soc.*, 2012, 134, 6751-6761.
64. S. Shuang, R. Lv, Z. Xie and Z. Zhang, 2016, 6, 26670.
65. S. Y. Chae, C. S. Lee, H. Jung, O.-S. Joo, B. K. Min, J. H. Kim and Y. J. Hwang, *ACS Appl. Mater. Interfaces*, 2017, 9, 19780-19790.
66. C. Sotelo-Vazquez, R. Quesada-Cabrera, M. Ling, D. O. Scanlon, A. Kafizas, P. K. Thakur, T.-L. Lee, A. Taylor, G. W. Watson, R. G. Palgrave, J. R. Durrant, C. S. Blackman and I. P. Parkin, *Adv. Funct. Mater.*, 2017, 27, 1605413-n/a.

67. V. B. R. Boppana and R. F. Lobo, *ACS Catal.*, 2011, 1, 923-928.
68. V. B. R. Boppana, F. Jiao, D. Newby, J. Laverock, K. E. Smith, J. C. Jumas, G. Hutchings and R. F. Lobo, *Phys. Chem. Chem. Phys.*, 2013, 15, 6185-6189.
69. J. Wang, H. Li, S. Meng, L. Zhang, X. Fu and S. Chen, *Appl. Catal., B*, 2017, 200, 19-30.
70. J. A. Libera, J. W. Elam, N. F. Sather, T. Rajh and N. M. Dimitrijevic, *Chem. Mater.*, 2010, 22, 409-413.
71. M. Nolan, A. Iwaszuk and H. Tada, *Aust. J. Chem.*, 2012, 65, 624-632.
72. Q. Jin, M. Fujishima and H. Tada, *J. Phys. Chem. C*, 2011, 115, 6478-6483.
73. Q. Jin, M. Fujishima, M. Nolan, A. Iwaszuk and H. Tada, *J. Phys. Chem. C*, 2012, 116, 12621-12626.
74. H.-Y. Chang, C.-C. Huang, K.-Y. Lin, W.-L. Kao, H.-Y. Liao, Y.-W. You, J.-H. Lin, Y.-T. Kuo, D.-Y. Kuo and J.-J. Shyue, *J. Phys. Chem. C*, 2014, 118, 14464-14470.
75. A. Iwaszuk, M. Nolan, Q. Jin, M. Fujishima and H. Tada, *J. Phys. Chem. C*, 2013, 117, 2709-2718.
76. D. S. Bhachu, S. Sathasivam, C. J. Carmalt and I. P. Parkin, *Langmuir*, 2014, 30, 624-630.
77. M. Fronzi, A. Iwaszuk, A. Lucid and M. Nolan, *J. Phys.: Condens. Matter*, 2016, 28, 074006.
78. M. Nolan, A. Iwaszuk, A. K. Lucid, J. J. Carey and M. Fronzi, *Adv. Mater.*, 2016, 28, 5425-5446.
79. Q. Jin, M. Fujishima, A. Iwaszuk, M. Nolan and H. Tada, *J. Phys. Chem. C*, 2013, 117, 23848-23857.
80. A. Iwaszuk and M. Nolan, *J. Mater. Chem. A*, 2013, 1, 6670-6677.
81. A. Iwaszuk and M. Nolan, *Catal. Sci. Technol.*, 2013, 3, 2000-2008.
82. A. Iwaszuk, A. K. Lucid, K. M. Razeeb and M. Nolan, *J. Mater. Chem. A*, 2014, 2, 18796-18805.
83. C. Di Valentin and A. Selloni, *J. Phys. Chem. Lett.*, 2011, 2, 2223-2228.
84. M. Nolan, *ACS Appl. Mater. Interfaces*, 2012, 4, 5863-5871.
85. Y. Ding and E. Alpay, *Chem. Eng. Sci.*, 2000, 55, 3929-3940.
86. Y. Ding and E. Alpay, *Chem. Eng. Sci.*, 2000, 55, 3461-3474.

87. M. J. Ramírez-Moreno, I. C. Romero-Ibarra, J. O. Landeros and H. Pfeiffer, in *CO2 Sequestration and Valorization*, eds. C. d. R. V. Morgado and V. P. P. Esteves, InTech, Rijeka, 2014, DOI: 10.5772/57444, p. Ch. 14.
88. K. Kim, J. W. Han, K. S. Lee and W. B. Lee, *Phys. Chem. Chem. Phys.*, 2014, 16, 24818-24823.
89. C. A. Downing, A. A. Sokol and C. R. A. Catlow, *Phys. Chem. Chem. Phys.*, 2014, 16, 184-195.
90. H.-J. Shin, J. Jung, K. Motobayashi, S. Yanagisawa, Y. Morikawa, Y. Kim and M. Kawai, *Nature Materials*, 2010, 9, 442.
91. J. Jung, H.-J. Shin, Y. Kim and M. Kawai, *Phys. Rev. B.*, 2010, 82, 085413.
92. Y. Duan and D. C. Sorescu, *J. Chem. Phys.*, 2010, 133, 074508.
93. H. Petitjean, C. Chizallet, J.-M. Krafft, M. Che, H. Lauron-Pernot and G. Costentin, *Phys. Chem. Chem. Phys.*, 2010, 12, 14740-14748.
94. H. S. Craft, R. Collazo, M. D. Losego, Z. Sitar and J. P. Maria, *Journal of Vacuum Science & Technology A: Vacuum, Surfaces, and Films*, 2008, 26, 1507-1510.
95. M. B. Jensen, L. G. M. Pettersson, O. Swang and U. Olsbye, *J. Phys. Chem. B*, 2005, 109, 16774-16781.
96. D. Ferry, S. Picaud, P. N. M. Hoang, C. Girardet, L. Giordano, B. Demirdjian and J. Suzanne, *Surf. Sci.*, 1998, 409, 101-116.
97. G. Pacchioni, J. M. Ricart and F. Illas, *J. Am. Chem. Soc.*, 1994, 116, 10152-10158.
98. M. Bajdich, J. K. Nørskov and A. Vojvodic, *Phys. Rev. B.*, 2015, 91, 155401.
99. J. A. McLeod, R. G. Wilks, N. A. Skorikov, L. D. Finkelstein, M. Abu-Samak, E. Z. Kurmaev and A. Moewes, *Phys. Rev. B.*, 2010, 81, 245123.
100. J. Carrasco, F. Illas and N. Lopez, *Phys. Rev. Lett.*, 2008, 100, 016101.
101. W. F. Schneider, *J. Phys. Chem. B*, 2004, 108, 273-282.
102. J. Jung, H.-J. Shin, Y. Kim and M. Kawai, *J. Am. Chem. Soc.*, 2011, 133, 6142-6145.
103. Z. Song, J. Fan and H. Xu, *Scientific Reports*, 2016, 6, 22853.
104. M. L. Granados, M. D. Z. Poves, D. M. Alonso, R. Mariscal, F. C. Galisteo, R. Moreno-Tost, J. Santamaría and J. L. G. Fierro, *Appl. Catal., B*, 2007, 73, 317-326.
105. N. H. de Leeuw and J. A. Purton, *Phys. Rev. B.*, 2001, 63, 195417.

106. B. Fubini, V. Bolis, M. Bailes and F. S. Stone, *Solid State Ionics*, 1989, 32-33, 258-272.
107. H. Manzano, R. J. M. Pellenq, F.-J. Ulm, M. J. Buehler and A. C. T. van Duin, *Langmuir*, 2012, 28, 4187-4197.
108. Y. Fujimori, X. Zhao, X. Shao, S. V. Levchenko, N. Nilius, M. Sterrer and H.-J. Freund, *J. Phys. Chem. C*, 2016, 120, 5565-5576.
109. H. Grönbeck and I. Panas, *Phys. Rev. B.*, 2008, 77, 245419.
110. C. J. Keturakis, F. Ni, M. Spicer, M. G. Beaver, H. S. Caram and I. E. Wachs, *ChemSusChem*, 2014, 7, 3459-3466.
111. G. Kresse and J. Hafner, *Phys. Rev. B.*, 1994, 49, 14251-14269.
112. G. Kresse and J. Furthmüller, *Computational Materials Science*, 1996, 6, 15-50.
113. G. Kresse and J. Furthmüller, *Phys. Rev. B.*, 1996, 54, 11169.
114. G. Kresse and D. Joubert, *Phys. Rev. B.*, 1999, 59, 1758-1775.
115. P. E. Blöchl, *Phys. Rev. B.*, 1994, 50, 17953-17979.
116. A. Lucid, A. Iwaszuk and M. Nolan, *Mater. Sci. Semicond. Process.*, 2014, 25, 59-67.
117. J. P. Perdew and Y. Wang, *Phys. Rev. B.*, 1992, 45, 13244-13249.
118. B. J. Morgan and G. W. Watson, *Phys. Rev. B.*, 2009, 80, 233102.
119. B. J. Morgan and G. W. Watson, *Surf. Sci.*, 2007, 601, 5034-5041.
120. M. Nolan and S. Rhatigan, *Chin. Chem. Lett.*, 2017, DOI: 10.1016/j.cclet.2017.11.036.
121. M. Nolan, *Chem. Commun.*, 2011, 47, 8617-8619.
122. M. Nolan, *Phys. Chem. Chem. Phys.*, 2011, 13, 18194-18199.
123. M. Nolan, A. Iwaszuk and K. A. Gray, *J. Phys. Chem. C*, 2014, 118, 27890-27900.
124. A. Iwaszuk, P. A. Mulheran and M. Nolan, *J. Mater. Chem. A*, 2013, 1, 2515-2525.
125. A. Iwaszuk and M. Nolan, *Phys. Chem. Chem. Phys.*, 2011, 13, 4963-4973.
126. A. D. Oliver and L. S. Alexander, *J. Phys.: Condens. Matter*, 2017, 29, 314005.
127. A. L. Shluger, K. P. McKenna, P. V. Sushko, D. M. Ramo and A. V. Kimmel, *Modell. Simul. Mater. Sci. Eng.*, 2009, 17, 084004.
128. A. M. Stoneham, J. Gavartin, A. L. Shluger, A. V. Kimmel, D. M. Ramo, H. M. Rønnow, G. Aeppli and C. Renner, *J. Phys.: Condens. Matter*, 2007, 19, 255208.
129. J. J. Carey and M. Nolan, *Catal. Sci. Technol.*, 2016, 6, 3544-3558.

130. S. Kwon, P. Liao, P. C. Stair and R. Q. Snurr, *Catal. Sci. Technol.*, 2016, 6, 7885-7895.
131. G. Henkelman, G. Jóhannesson and H. Jónsson, in *Theoretical Methods in Condensed Phase Chemistry*, Springer, 2002, pp. 269-302.
132. G. Henkelman, B. P. Uberuaga and H. Jónsson, *J. Chem. Phys.*, 2000, 113, 9901-9904.
133. D. Fernández-Torre, K. Kośmider, J. Carrasco, M. V. Ganduglia-Pirovano and R. Pérez, *J. Phys. Chem. C*, 2012, 116, 13584-13593.
134. J. Carrasco, D. López-Durán, Z. Liu, T. Duchoň, J. Evans, S. D. Senanayake, E. J. Crumlin, V. Matolín, J. A. Rodríguez and M. V. Ganduglia-Pirovano, *Angew. Chem. Int. Ed.*, 2015, 54, 3917-3921.
135. S. Fuente, M. M. Branda and F. Illas, *Theor. Chem. Acc.*, 2012, 131, 1190.
136. D. Marrocchelli and B. Yildiz, *J. Phys. Chem. C*, 2012, 116, 2411-2424.
137. P. J. D. Lindan and C. Zhang, *Phys. Rev. B.*, 2005, 72, 075439.
138. P. M. Kowalski, B. Meyer and D. Marx, *Phys. Rev. B.*, 2009, 79, 115410.
139. L. Yang, D.-J. Shu, S.-C. Li and M. Wang, *Phys. Chem. Chem. Phys.*, 2016, 18, 14833-14839.
140. J. B. Park, J. Graciani, J. Evans, D. Stacchiola, S. D. Senanayake, L. Barrio, P. Liu, J. F. Sanz, J. Hrbek and J. A. Rodriguez, *J. Am. Chem. Soc.*, 2010, 132, 356-363.
141. J. A. Rodríguez, J. Evans, J. Graciani, J.-B. Park, P. Liu, J. Hrbek and J. F. Sanz, *J. Phys. Chem. C*, 2009, 113, 7364-7370.
142. B. H. Solis, Y. Cui, X. Weng, J. Seifert, S. Schauermann, J. Sauer, S. Shaikhutdinov and H.-J. Freund, *Phys. Chem. Chem. Phys.*, 2017, 19, 4231-4242.



Rutile TiO_2 modified with alkaline earth oxide nanoclusters promotes water activation and capture of CO_2.